BMC Microbiology

RESEARCH

Open Access

Rosmarinic Acid inhibits Pseudorabies Virus (PRV) infection by activating the cGAS-STING signaling pathway

Tingting Hu[1†], Sihui Gao[1†], Zhijie Yu[1], Yunhao Liu[1], Huaqiao Tang[1], Zhiwen Xu[1], Ling Zhu[1], Ling Zhao[1], Gang Ye[1] and Fei Shi[1*]

Abstract

Pseudorabies virus (PRV), a swine alphaherpesvirus, is a double-stranded DNA virus. It may infect various animals, especially pigs. PRV infection in pigs leads to high mortality rates, and causes huge economic lose for swine industry. Currently, there are few effective antiviral treatments available. Rosmarinic acid (RA), a hydrophilic phenolic compound, shows potential for inhibiting herpes simplex virus. Given that PRV is a member of the *Herpesviridae* family, this study investigated the antiviral effects of RA against PRV infection through both in vitro and in vivo, as well as the underlying molecular mechanisms. PK-15 cells were used to assess the cytotoxicity of RA in vitro, followed by an investigation of its anti-PRV activity. The study then explored how RA regulates the cGAS-STING signaling pathway, along with inflammatory and apoptotic factors in PRV-infected cells. Molecular docking and dynamics simulations further elucidated the binding interactions between RA and cGAS-STING, providing insight into how RA activates the cGAS-STING pathway against PRV infection. In vivo, the antiviral efficacy of RA was evaluated in a PRV-infected mouse model by assessing tissue viral genome copies, the innate immune cGAS-STING signaling pathway activation, and inflammatory and apoptotic responses. The results showed that RA exhibited a half-maximal cytotoxic concentration (CC_{50}) of 26.23 μg/mL on PK-15 cells and a half-maximal inhibitory concentration (IC_{50}) of 0.84 μg/mL against PRV, resulting in a selectivity index (SI) of 31.22. These findings suggest that RA is a highly effective and low-toxicity compound. RA significantly inhibited PRV adsorption, penetration, and replication within cells. Additionally, while PRV infection suppresses the cGAS-STING signaling pathway, RA treatment activates the innate immune response, enhances downstream antiviral effector IFN-β expression, and reduces inflammation and apoptosis in PRV-infected cells. Molecular docking results showed that the docking scores of cGAS_RA and STING_RA complexes were both less than −5 kcal/mol, suggesting that RA binds well to cGAS and STING proteins. Molecular dynamics simulations, including RMSD, RMSF, and MM-GBSA analyses, confirmed the high binding stability of cGAS with RA, further validating the potential activity of RA as a cGAS agonist. In vivo studies revealed that RA dramatically lowered viral genome copies in various organs, activated the cGAS-STING signaling pathway, inhibited PRV-induced inflammation and apoptosis, alleviated clinical symptoms, and decreased mortality rate in PRV-infected mice. Overall, RA significantly inhibited PRV proliferation in vitro and in vivo, effectively reduced inflammation and apoptosis, and decreased

†Tingting Hu and Sihui Gao contributed equally to this work.

*Correspondence:
Fei Shi
fei_shi@sicau.edu.cn
Full list of author information is available at the end of the article

© The Author(s) 2025. **Open Access** This article is licensed under a Creative Commons Attribution-NonCommercial-NoDerivatives 4.0 International License, which permits any non-commercial use, sharing, distribution and reproduction in any medium or format, as long as you give appropriate credit to the original author(s) and the source, provide a link to the Creative Commons licence, and indicate if you modified the licensed material. You do not have permission under this licence to share adapted material derived from this article or parts of it. The images or other third party material in this article are included in the article's Creative Commons licence, unless indicated otherwise in a credit line to the material. If material is not included in the article's Creative Commons licence and your intended use is not permitted by statutory regulation or exceeds the permitted use, you will need to obtain permission directly from the copyright holder. To view a copy of this licence, visit http://creativecommons.org/licenses/by-nc-nd/4.0/.

the mortality rate in infected mice. The study supports the development of RA as an antiviral drug and emphasizes its potential as a candidate for PRV therapy.

Keywords Pseudorabies virus (PRV), Rosmarinic acid (RA), Antiviral activity, CGAS-STING

Introduction

Pseudorabies virus (PRV) is a DNA virus that belongs to the *Herpesviridae* family. It was first identified in the United States and has spread. Although PRV primarily infects pigs, it can also cause fatal diseases in other mammals, including cattle, sheep, dogs, and cats. PRV infection in pigs causes neurological symptoms, respiratory illness, abortions, and high mortality rates in newborn piglets [1, 2]. The widespread use of the gE-deleted Bartha-K61 vaccine has effectively controlled traditional PRV strains. However, the ongoing emergence of wild-type and mutant strains continues to threaten the global swine industry, which underscores the urgent need for more effective vaccines and therapeutic interventions [3, 4].

Rosmarinic acid (RA), a water-soluble natural polyphenol, is widely found in various plants, and it is known for its anti-inflammatory, antioxidant, antitumor, antimicrobial, and antiviral pharmacological activities [5–8]. Recent research has extensively explored its antiviral properties, revealing that RA inhibits HBV replication in cells by targeting the ε-Pol binding interaction [9]. In vitro studies demonstrate that RA inhibits multiple strains of influenza A virus (IAV), including oseltamivir-resistant mutants, by reducing GSK3β and phosphorylated AKT levels, thus disrupting viral entry and replication. In vivo, RA significantly improves survival and prevents weight loss in IAV-infected mice [10]. Furthermore, RA alleviates severe lung damage induced by the H1N1 virus by activating the h-PGDS-PGD2-HO-1 signaling pathway [11]. RA also reduces mortality and viral genome copies in Japanese encephalitis virus (JEV)-infected mice, along with lowering pro-inflammatory cytokine levels [12]. Notably, RA shows great efficacy against type I and type II herpes simplex viruses. For instance, it prevents herpes simplex virus type 1 (HSV-1) infection by targeting ALOX15 to suppress lipid peroxidation, restoring STING-mediated innate immune function and reducing HSV-1 susceptibility in vitro and in vivo [13].

Innate immunity serves as the initial defense line, providing a rapid and nonspecific response to pathogens. The DNA sensor cGAS is an important part of this defensive system. Cyclic GMP-AMP synthase (cGAS) is an intracellular DNA sensor that detects and binds viral DNA [14]. Upon DNA virus infection, cGAS recognizes viral DNA in the cytoplasm, changes conformation, and catalyzes the synthesis of cyclic GMP-AMP (cGAMP). cGAMP acts as a secondary messenger, binding to and activating the endoplasmic reticulum's stimulator of interferon genes (STING) [15]. The activation of STING drives cGAMP translocate from the ER to the Golgi apparatus, where it interacts with signaling molecules. Once activated, STING recruits and stimulates downstream signaling molecules such as TANK-binding kinase 1 (TBK1) [16] and IκB kinase ε (IKKε), leading to the activation of the transcription factor interferon regulatory factor 3 (IRF3). The activated IRF3 then translocates to the nucleus to initiate the expression of type I interferon (IFN-β). The release of IFN-β is a crucial function of the cGAS-STING pathway in antiviral defense. IFN-β not only induces an antiviral state in infected cells but also enhances the activation of immune cells like macrophages, NK cells, and T cells, thereby strengthening systemic antiviral immunity [17]. Activation of the cGAS-STING pathway helps clear infected cells, suppress viral replication, and establish an antiviral state to prevent further spread [18, 19]. However, research indicates that many viruses, particularly DNA viruses, have evolved mechanisms to evade host immune surveillance by targeting the cGAS-STING signaling pathway. For example, the HSV-1 UL37 protein suppresses pathway activation by mediating the deamidation of cGAS [20]. The HSV-1 UL41 protein degrades cGAS via its RNase activity, thereby reducing the accumulation of cGAS to abrogate host recognition of viral DNA [21]. Degradation of β-arrestin 2 induced by viral infection also results in the suppression of the cGAS-STING pathway [22]. Additionally, the HSV-1 VP1-2 protein facilitates viral immune evasion by deubiquitinating STING [23]. The HSV-1 VP24 protein can also inhibit the activation of IRF3 to block the production of IFN-β [24].

PRV belonging to the *Herpesviridae* family has developed multiple immune evasion strategies to counteract the host antiviral response. For instance, the PRV tegument protein UL13 suppresses antiviral signaling by modulating STING stability [25, 26], PRV UL13 effectively inhibits cGAS-STING-mediated IFN-β production by phosphorylating activated IRF3 and disrupting IRF3 binding to the IRF3-responsive promoter [26]. Additionally, PRV UL38 protein suppresses the cGAS-STING pathway by degrading STING via autophagy, thereby reducing the activation of IFN-β [27]. PRV US2 selectively targets STING to inhibit IFN signaling, effectively evading the host antiviral response [28]. PRV gE

can inhibit cGAS-STING-mediated IFN-β production by degrading CBP, thereby disrupting the enhanced assembly of IRF3 with CBP [29].

In summary, PRV presents an unavoidable challenge to the global swine industry. Despite advances in vaccine development, effective treatments remain limited, underscoring the need to explore economical and effective antiviral agents derived from natural sources. Preliminary studies suggest that RA exhibits antiviral activity against herpesviruses, warranting further investigation into its potential efficacy and mechanisms against PRV. This study evaluated the effectiveness of RA in inhibiting PRV both in vitro and in vivo, as well as its modulation of the cGAS-STING innate immune pathway, offering new insights for the development of the antiviral drug.

Materials and methods

Cells, virus

PK-15 cells (CCTCC GDC0061) were sourced from the China Center for Type Culture Collection (CCTCC) and cultured in DMEM (Gibco, Waltham, MA, USA) supplemented with 10% FBS (Vazyme, Wuhan, China) at 37 °C with 5% CO_2. During the viral experiment, the cell maintenance medium consisted of DMEM supplemented with 2% FBS. The PRV-Ra strain (CVCC AV25) was maintained in the China Veterinary Culture Collection Center (CVCC) and propagated in PK-15 cells. Virus virulence was measured as the median tissue culture infective dose ($TCID_{50}$) [30].

Animals

Six weeks old male ICR mice were purchased from SPF (Beijing) biotechnology Co. Ltd. (Beijing, China). All animal procedures were approved by the Animal Protection and Experimental Ethics Committee of Sichuan Agricultural University (Sichuan, China, approval No.20230045).

Compounds and reagents

Rosmarinic acid (RA, HPLC ≥ 98%) was obtained from Shanghai Yuanye Bio-Technology Co., Ltd. (Shanghai, China). ELISA kits for TNF-α, IL-1β, IL-6, Caspase-3, BAX, and BCL-2 were procured from Quanzhou Ruixin Biological Technology Co., Ltd. (Quanzhou, China). Antibodies for Western blot analysis were acquired from ABclonal Technology (Wuhan, China). All other chemicals and reagents were purchased from standard commercial suppliers.

Cytotoxicity assay

PK-15 cell cultures were treated with varying concentrations of RA (50, 25, 12.5, 6.25, and 3.125 μg/mL) and incubated at 37 °C for 48 h. The DMSO content was strictly controlled to not exceed 0.5% in all treatments. Cell viability was assessed using the Cell Counting Kit-8 (CCK-8) (Vazyme, Nanjing, China). The 50% cytotoxic concentration (CC_{50}) was calculated using GraphPad Prism 9.5.1 software [31].

Virus titration

PK-15 cells in 96-well plates were infected with ten-fold serial dilutions of PRV. After 1 h stewing at 37 °C, the culture medium was replaced with fresh cell maintenance medium. Cytopathic effects (CPE) were observed and recorded at 48 h post-inoculation (hpi), and the 50% tissue culture infectious dose ($TCID_{50}$) was calculated using the Reed-Muench method [30, 32].

Antiviral activity of RA against PRV in vitro

RA was diluted to five concentrations (6, 3, 1.5, 0.75, and 0 μg/mL), and a 100 $TCID_{50}$ dose of PRV was inoculated onto PK-15 cell monolayers in 96-well plates. After 1 h of adsorption, the virus was removed, and cells were washed three times with sterile PBS. Fresh maintenance medium was added, and cells were incubated for 48 h at 37 °C with 5% CO_2. The CPE were observed at 48 hpi. Cell viability was then assessed using the CCK8 assay to evaluate the protective effect of RA on infected cells, indirectly indicating its inhibition of PRV replication. Normalized to 0 μg/mL treatment (cell viability 0%, PRV inhibition 0%). The 50% inhibitory concentration (IC_{50}) was calculated using GraphPad Prism 9.5.1 software, and the selectivity index (SI) was determined as the ratio of CC_{50} to IC_{50} [31].

Transmission electron microscopy (TEM) observation of cellular lesions in PK-15 cells

PK-15 cells were cultivated in 6-well plates and separated into three groups: MOCK, PRV, and RA treatment. Both the PRV and RA treatments were infected with 100 $TCID_{50}$ of PRV and incubated for 1 h at 37 °C. The cells were then washed three times with sterile PBS. The MOCK and PRV groups received fresh cell maintenance medium, while the RA treatment group was supplemented with 6 μg/mL of RA. After 48 hpi, cells were observed using light microscopy (Leica, Wetzlar, Germany). To assess ultrastructural damage from viral infection, PK-15 cells were prefixed with 3% glutaraldehyde, postfixed with 1% osmium tetroxide, dehydrated in a graded acetone series, infiltrated with Epon 812, and embedded. Semithin sections were dyed with methylene blue, and ultrathin sections were cut using a diamond knife and stained with uranyl acetate and lead citrate. The slices were then observed with a JEM-1400-FLASH transmission electron microscope (JEOL, Tokyo, Japan). Initial grid viewing was performed at 8000x magnification, with

selected images captured for detailed analysis of specific cellular lesions.

Direct interaction between RA and PRV

To assess whether RA directly interacts with PRV to reduce viral titers, PRV (200 $TCID_{50}$) and RA (12 μg/mL) were mixed in a centrifuge tube. A control with 100 $TCID_{50}$ of PRV was included to account for temperature effects on viral potency. All tubes were incubated at 37 °C with 5% CO_2 for 1 h, then added to PK-15 cell monolayers in 6-well plates and incubated at 37 °C for 1 h. The cells were washed three times with sterile PBS, and fresh maintenance medium was added. Supernatant and cell samples were collected at 48 hpi for viral genome copies assessment using quantitative real-time PCR (qRT-PCR).

Time of addition assay

To determine which step of the PRV life cycle is impacted by RA, the RA was administered before (pre-treatment), during (co-treatment), or after (post-treatment) PRV infection [33]. In the pre-treatment group, cells were exposed to RA (6 μg/mL) for 1 h before inoculation with 100 $TCID_{50}$ of PRV. The co-treatment group got RA (6 μg/mL) concurrently with PRV infection, while the post-treatment group was given RA (6 μg/mL) 1 h after PRV inoculation. Supernatant and cell samples were collected at 48 hpi for viral genome copies assessment using qRT-PCR.

Impact of RA on PRV growth activity

PK-15 cells grown to confluence 70–80% in 6-well plates were inoculated with PRV (1000 $TCID_{50}$) and incubated at 37 °C for 1 h. The viral suspension was removed, and cells were washed three times with sterile PBS. RA-treated groups were then exposed to a 6 μg/mL RA solution, while the PRV groups received fresh cell maintenance medium. The plates were incubated at 37 °C with 5% CO_2. Supernatant and cell samples were collected at 3, 6, 9, 12, 16, and 24 h post-treatment for qRT-PCR analysis.

Viral genome copies determination and qRT-PCR

Viral DNA was extracted using the FastPure® Viral DNA/RNA Mini Kit (Vazyme, Nanjing, China). Absolute quantification of viral DNA was performed using a standard curve method based on the DNA sequence of the PRV gB gene (Gene ID: 80532586). Standard plasmids were constructed, and viral copy numbers were calculated by comparing the fluorescence signals of samples with the standard curve [34].

PK-15 cells were seeded onto 6-well plates and grown into a monolayer. The PRV and the RA treatment groups were infected with 100 $TCID_{50}$ PRV and incubated at 37 °C for 1 h. Subsequently, cells were washed three times with sterile PBS. The PRV and MOCK groups were received fresh cell maintenance medium, while the RA treatment group was given 6 μg/mL of RA. Cells were collected after 48 h of incubation. Total RNA was extracted using the EASYspin Plus Tissue/Cell RNA Rapid Extraction Kit (Aidlab, Beijing, China), and reverse transcribed into cDNA using the HiScript III All-in-one RT SuperMix Perfect for qPCR (Vazyme, Wuhan, China). qRT-PCR was performed with ChamQ SYBR qPCR Master Mix (Vazyme, Wuhan, China). Gene expression levels were normalized to β-actin and analyzed relative to the MOCK using the $2^{-\Delta\Delta CT}$ method. Each reaction was carried out in triplicate. The primer sequences are presented in Table 1. Primers were synthesized by Chengdu Youkang Jianxing Biotechnology Co., Ltd.(Chengdu, China), and the positive control plasmid for the PRV gB gene was synthesized by Sangon Biotech Co., Ltd (Shanghai, China).

Western blot

PK-15 cells were seeded in 6-well plates and grown to confluence. The PRV and RA treatment groups were infected with 100 $TCID_{50}$ PRV and incubated at 37 °C for 1 h. Afterward, cells were washed three times with sterile PBS. The PRV group and MOCK group were received fresh cell maintenance medium, whereas the RA treatment group was given 6 μg/mL of RA. After 24 h of incubation, cells were lysed on ice with cold RIPA complete lysis buffer (Beyotime, Shanghai, China) supplemented with 1 mM PMSF (Beyotime, Shanghai, China). The lysates were centrifuged at 12,000 × g to collect the supernatant, and protein concentrations were determined using a BCA protein assay kit (Vazyme, Wuhan, China). The protein samples were mixed with 5× SDS-PAGE sample loading buffer (Beyotime, Shanghai, China) and incubated at 95 °C for 10 min. Protein separation was performed by 4–12% SDS-PAGE, followed by transfer to PVDF membranes (Millipore, Merck, USA) using a Bio-Rad transfer apparatus. The membranes were blocked with 5% non-fat milk in TBS containing 0.1% Tween-20 (TBST) at room temperature for 2 h, then incubated overnight with primary antibodies at 4 °C. After three washes with TBST, membranes were incubated with secondary antibodies at room temperature for 1 h. Protein bands were detected using the SuperFemto ECL chemiluminescence kit (Vazyme, Wuhan, China). The expression levels of β-actin and proteins involved in the cGAS-STING pathway were assessed by western blotting [35]. Grayscale values of protein bands were analyzed using a Bio-Rad ChemiDoc MP imaging system (Bio-Rad, USA) and quantified with Image J software (NIH, USA) [36].

Table 1 Lists the primers used in the qRT-PCR analysis

Primers	Sequence(5′→3′)	Accession number
PRV-UL27-F PRV-UL27-R	ACAAGTTCAAGGCCCACATCTAC GTCTGTGAAGCGGTTCGTGAT	NC_075689.1
pTNF-α-F pTNF-α-R	CGACTCAGTGCCGAGATCAA CCTGCCCAGATTCAGCAAAG	NM_214022.1
pIL-1β-F pIL-1β-R	AGAATCTCAGAAACCCGACTGTTT TTCAGCAACACGGGTTCGT	NM_001302388.2
pIL-6-F pIL-6-R	ATTAAGTACATCCTCGGCAAA GTTTTCTGCCAGTACCTCC	NM_214399.1
pCaspase-3-F pCaspase-3-R	AAGACCATAGCAAAAGGAGCA GTTCACAGCAGTCCCCTC	NM_214131.1
pBax-F pBax-R	GTTTCATCCAGGATCGAGCA TGCAGCTCCATGTTACTGTCC	XM_003127290.5
pBcl-2-F pBcl-2-R	CTGCACCTGACTCCCTTCACC TCCCGGTTGACGCTCTCCACA	XM_021099593.1
pβ-actin-F pβ-actin-R	GGACTTCGAGCAGGAGATGG AGGAAGGAGGGCTGGAAGAG	AJ312193.1
mcGAS-F mcGAS-R	CACCTCTGCTCTGTTACCCTTGG ACGCTTCTGTTCAATCACTTGGATG	NM_173386.5
mSTING-F mSTING-R	AACTGCCGCCTCATTGTCTACC CATGCTGCTGCCCTATCTCCTG	NM_001289592.1
mIRF3-F mIRF3-R	GGGCGGACCTTGGAATATTAG CCAGGACACTCTTCGTCATTAG	NM_016849.4
mIFN-β-F mIFN-β-R	TCCGAGCAGAGATCTTCAGGAA TGCAACCACCACTCATTCTGAG	NM_010510.2
mTNF-α-F mTNF-α-R	CCAGACCCTCACACTCACAAACC CAGCCTTGTCCCTTGAAGAGAACC	NM_001278601.1
mIL-1β-F mIL-1β-R	CACTACAGGCTCCGAGA GCCACAGGTATTTTGTCGTT	NM_008361.4
mIL-6-F mIL-6-R	GTCGGAGGCTTAATTACACA CAAGTGCATCATCGTTGT	NM_001314054.1
mCaspase-3-F mCaspase-3-R	GACGCAGCCAACCTCA ACCATGGCTTAGAATCACAC	NM_009810.3
mBax-F mBax-R	TTTCATCCAGGATCGAGCAG CACGTCAGCAATCATCCTC	NM_001411994.1
mBcl-2-F mBcl-2-R	ACCTGACGCCCTTCACC CATCTCCCTGTTGACGCTCT	NM_177410.3
mβ-actin-F mβ-actin-R	GCAAGCAGGAGTACGATGAGT GGTGTAAAACGCAGCTCAGTA	NM_007393.5

The UL27 gene of PRV encodes glycoprotein B (gB); p means pig and m means mouse

Molecular docking and molecular dynamics simulation

Using Schrödinger software, the 3D structure of Rosmarinic acid (RA, PubChem CID: 5281792) was prepared by the Ligprep module, with stereoisomers and protonation states optimized by the Epik module. The STING protein structure, predicted by AlphaFold2 (Accession No. K7GKX5), was used due to the lack of an experimentally resolved crystal structure. For cGAS (PDB ID: 4JLZ), a high-resolution crystal structure bound to a small molecule was selected. Protein preparation was carried out utilizing Schrödinger's Protein Preparation Wizard module. Molecular docking was performed using the Glide module with GlideScore as the scoring function. For each docking simulation, ten conformations per ligand were created and minimized, with the best-scoring conformation chosen for future investigation. The protonation states of protein residues were calculated using PROPKA 3.0, retaining all initial crystallographic water molecules in the selected crystal structure. The full-atom complex model was built using the System Builder module in Schrödinger, parameterized with the OPLS_4 force field for both protein and ligand, and the TIP3P model for water, with a boundary thickness of 10.0 Å. During the simulation, trajectory energy and coordinates were saved every 10 ps. Post-simulation, interaction modes and dynamic trajectory animations were analyzed using Schrödinger 2022, with RMSD and RMSF calculated to assess structural stability. Finally, a stable snapshot was selected to analyze the binding mode of the protein-ligand complex and calculate the MM-GBSA binding free energy [37, 38].

In vivo assessment of RA efficacy

Determination of LD50

After an acclimation period, forty 6-week-old male ICR mice were randomly assigned into five groups ($n=8$ each). Viral stock was serially diluted ten-fold to create concentrations ranging from 10^{-2} to 10^{-6}. Each group received a 0.1 mL intraperitoneal injection of the respective viral dilution. Mortality rates were monitored for 5 days post-injection, and the LD_{50} was determined using the Reed-Muench method.

Mouse infection model and treatments

Fifty ICR mice were acclimatized for one week and then randomly allocated to five groups ($n=10$ each): a blank control group (MOCK), a virus control group (PRV), a low-dose RA treatment group (25 mg/kg, RA-L), a medium-dose RA treatment group (50 mg/kg, RA-M), and a high-dose RA treatment group (100 mg/kg, RA-H). RA dose schedules were based on previously published reports [11, 39, 40]. The PRV and RA-L/M/H groups were intraperitoneally injected with 0.1 mL of $10^{-4.2}$ PRV solution, while the MOCK group got an equivalent volume of sterile saline. With the PRV infection challenge, the RA-H, RA-M, and RA-L groups administered RA daily by oral gavage for 5 consecutive days, depending on preliminary dosage optimization. The MOCK and PRV groups were received an equivalent volume of sterile saline daily. Clinical symptoms and mortality were documented daily. Survival rates were determined using the Reed-Muench method. After 5 days, all mice were euthanized using a gradual-fill CO_2 system, with CO_2 introduced at approximately 20% of the chamber volume per minute, in accordance with animal welfare guidelines. The mice lost consciousness gradually, minimizing

discomfort. Liver, kidneys, spleen, brain, lungs, duodenum, jejunum, ileum, and cecum tissues were collected and stored at −80 °C for further analysis.

Measurement of PRV genome copies in mouse tissues

Liver, kidneys, spleen, brain, lungs, duodenum, jejunum, ileum, and cecum tissues were dissected from six mice per group. A 100 mg tissue sample was weighed, homogenized in 1 mL PBS using a tissue homogenizer until no tissue clumps remained, and then centrifuged briefly to collect the supernatant. Viral DNA was extracted from the homogenized supernatant using the FastPure® Viral DNA/RNA Mini Kit (Vazyme, Nanjing, China) and quantified by qRT-PCR with a standard curve to determine viral genome copies.

Assessment of RA effects on apoptosis and inflammatory factors in PRV-infected mice

Lung tissue was homogenized and centrifuged to obtain the supernatant, and tested for TNF-α, IL-1β, IL-6, Caspase-3, BAX levels with ELISA kits.

Statistical analysis

All data were presented as means ± SD and analyzed using GraphPad Prism (version 9.5.1) for statistical tests and visualization, including t-tests, one-way ANOVA, and two-way ANOVA. p-values less than 0.05 were considered statistically significant, with significance levels indicated as follows: $^{*}p < 0.05$, $^{**}p < 0.01$, $^{***}p < 0.001$, and $^{****}p < 0.0001$.

Results

RA significantly inhibits PRV-induced cellular lesions in PK-15 cells

PK-15 cells were treated with various concentrations of RA for 48 h to assess cytotoxicity and antiviral efficacy using the CCK-8 assay. RA had no obvious cytotoxicity when the concentration was less than 6.25 μg/mL. The CC_{50} value of RA for PK-15 cells was determined to be 26.23 μg/mL (Fig. 1A), and the IC_{50} value was 0.84 μg/mL (Fig. 1B). The SI calculated as CC_{50}/IC_{50}, was 31.22, indicating that RA is highly effective with low toxicity.

After 48 h of incubation, microscopic observation revealed that MOCK cells were well-adhered, and exhibited normal morphology. In contrast, PRV-infected cells

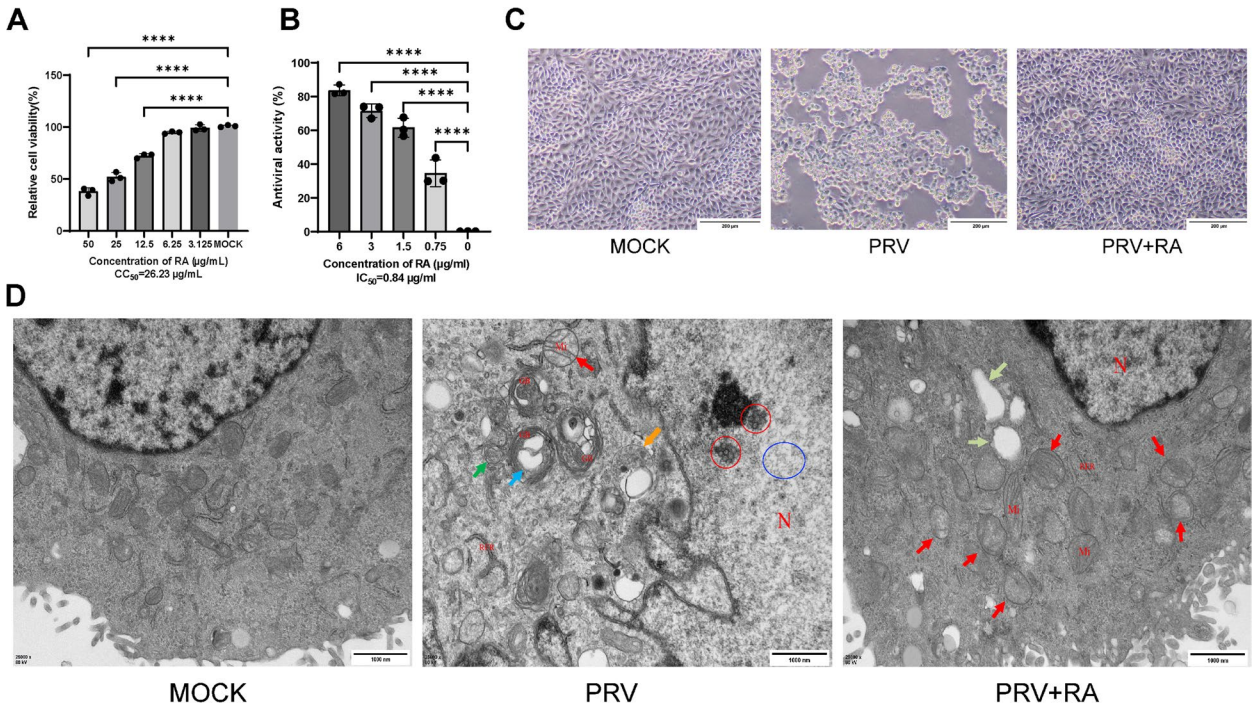

Fig. 1 RA effectively inhibits PRV infection in PK-15 cells. **A** Cytotoxicity of RA on PK-15 cells. **B** The inhibitory effect of RA on PRV. **C** RA mitigated cell damage induced by PRV, as observed through light microscopy. Magnification: ×200. Scale bar, 200 μm. **D** RA reduced the ultrastructural damage in PK-15 cells infected with PRV, as observed through TEM. Observations included virus (○), nucleus (N), mitochondria (Mi), rough endoplasmic reticulum (RER), Golgi apparatus (GB); mild loss of chromatin (○); mitochondrial swelling(↑); autophagic lysosomes (↑); ring-shaped Golgi apparatus with mildly expanded vesicles (↑); and multivesicular bodies(↑); vacuoles (↑). Magnification: ×25,000. Scale bar, 1000 nm. Statistical analyses were performed using one-way ANOVA, followed by Dunnett's post-hoc test. p-values less than 0.05 were considered statistically significant ($^{*}p < 0.05$, $^{**}p < 0.01$, $^{***}p < 0.001$ and $^{****}p < 0.0001$ compared with the control group)

showed significant pathological changes, including extensive shrinkage, rounding, and detachment. RA-treated cells (PRV + RA) exhibited markedly fewer pathological changes compared to the PRV-infected cells (Fig. 1C).

TEM revealed ultrastructural damage caused by viral infection. Cells in the MOCK group appeared larger, and rounded, with oval nuclei, evenly distributed chromatin, minimal heterochromatin, intact nuclear membranes, and visible organelles, including elongated or ovoid mitochondria, a well-defined rough endoplasmic reticulum with parallel double membranes, and distinct Golgi apparatus. In contrast, PRV-infected cells displayed significant morphological changes, including irregular nuclei with chromatin loss, damaged nuclear envelopes, and clustered viral particles. Mitochondria showed swelling, matrix dissolution, vacuolation, and sparse, irregular cristae. The rough endoplasmic reticulum was also disrupted, and the cell membrane was ruptured. PRV infected cells treated with RA exhibited less damage compared to the PRV group, with oval nuclei, evenly distributed chromatin, intact nuclear envelopes, and rounded or rod-shaped mitochondria with clear cristae. Mild swelling, matrix dissolution, and decreased electron density were observed in some mitochondria, but the outer membrane remained intact. The rough endoplasmic reticulum maintained its organization, and the cell membrane and microvilli appeared normal (Fig. 1D).

RA significantly inhibits PRV adsorption, penetration, and replication

A time-of-addition assay (Fig. 2A) was designed to assess the effects of RA on different stages of the PRV life cycle, including adsorption (pre-treatment), penetration (co-treatment), replication (post-treatment), and direct inactivation. The results revealed that RA did not exhibit significant direct virucidal activity against PRV (Fig. 2E), but it effectively inhibited viral adsorption (Fig. 2B), penetration (Fig. 2C), and replication (Fig. 2D). Growth curve analysis (Fig. 2F) further confirmed the inhibitory effect of RA on PRV replication. Notably, the viral genome copies in RA-treated cells were markedly lower than those in the PRV group at 12 h post-infection.

RA upregulates the cGAS-STING signaling pathway and the antiviral effector IFN-β

To further elucidate the antiviral mechanism of RA, western blotting was employed to evaluate the expression of cGAS-STING and IFN-β genes [41]. Compared to the MOCK group, PRV decreased the expression of cGAS (Fig. 3A), STING (Fig. 3B), and IFN-β (Fig. 3D) proteins, inhibited phosphorylation of IRF3 (Fig. 3C). RA treatment counteracted the inhibition, thereby enhancing signal transduction and activating the antiviral immune response.

RA indicated high binding stability with cGAS

Molecular docking and molecular dynamics simulations were employed to investigate the interaction mechanism between RA and the proteins of cGAS and STING. The binding affinity between the small molecule and its protein targets was calculated with docking scores. Typically, binding energy below −5 kcal/mol suggests potential docking, with lower values indicating more stable interactions [31]. The molecular docking scores for RA with cGAS and STING were −6.346 kcal/mol (Fig. 4A) and −6.516 kcal/mol (Fig. 4B), respectively, suggesting strong binding affinities [39, 42, 43], These results were further substantiated by positive and negative control docking experiments, which confirmed the reliability of the binding interactions (Figure S1).

Molecular dynamics simulations were used to design the module of the Schrödinger drug design suite. Following 100 ns of simulation, we calculated the root mean square deviation (RMSD) and root mean square fluctuation (RMSF) for the entire trajectory of the complex. A snapshot from the stable state was then selected for molecular mechanics generalized born surface area (MM-GBSA) binding free energy analysis and energy decomposition.The RMSD analysis revealed that the cGAS_RA complex exhibited minor fluctuations, ranging from approximately 1.2 to 2.4 Å, indicating overall stability, with equilibrium reached after 40 ns at an RMSD of about 2 Å (Fig. 4C). In contrast, the STING_RA complex displayed larger fluctuations, between 4.5 and 10.5 Å, likely due to its flexible protein structure with multiple loops, stabilizing around 10.5 Å after 60 ns (Fig. 4D). RMSF results showed that the cGAS_RA complex maintained low fluctuations, except for a region spanning amino acids 225–250, which fluctuated up to 4.0 Å, corresponding to a peripheral protein region distant from the binding pocket, thus not affecting ligand binding stability (Fig. 4E). The STING_RA complex exhibited greater fluctuations, mostly above 3.0 Å, with notable peaks at amino acids 0–25 and 270–283, corresponding to flexible N- and C-terminal regions, which are also distant from the binding pocket and do not impact binding stability (Fig. 4F).

The binding free energy reflects the interaction strength between the ligand and receptor [44]. MM-GBSA analysis of the final stable snapshots for both cGAS and STING complexes indicated strong binding, with the STING_RA complex showing the highest binding free energy (Fig. 4G). Collectively, the RMSD, RMSF, and MM-GBSA analyses suggest that the cGAS_RA complex is particularly stable, outperforming the STING complex.

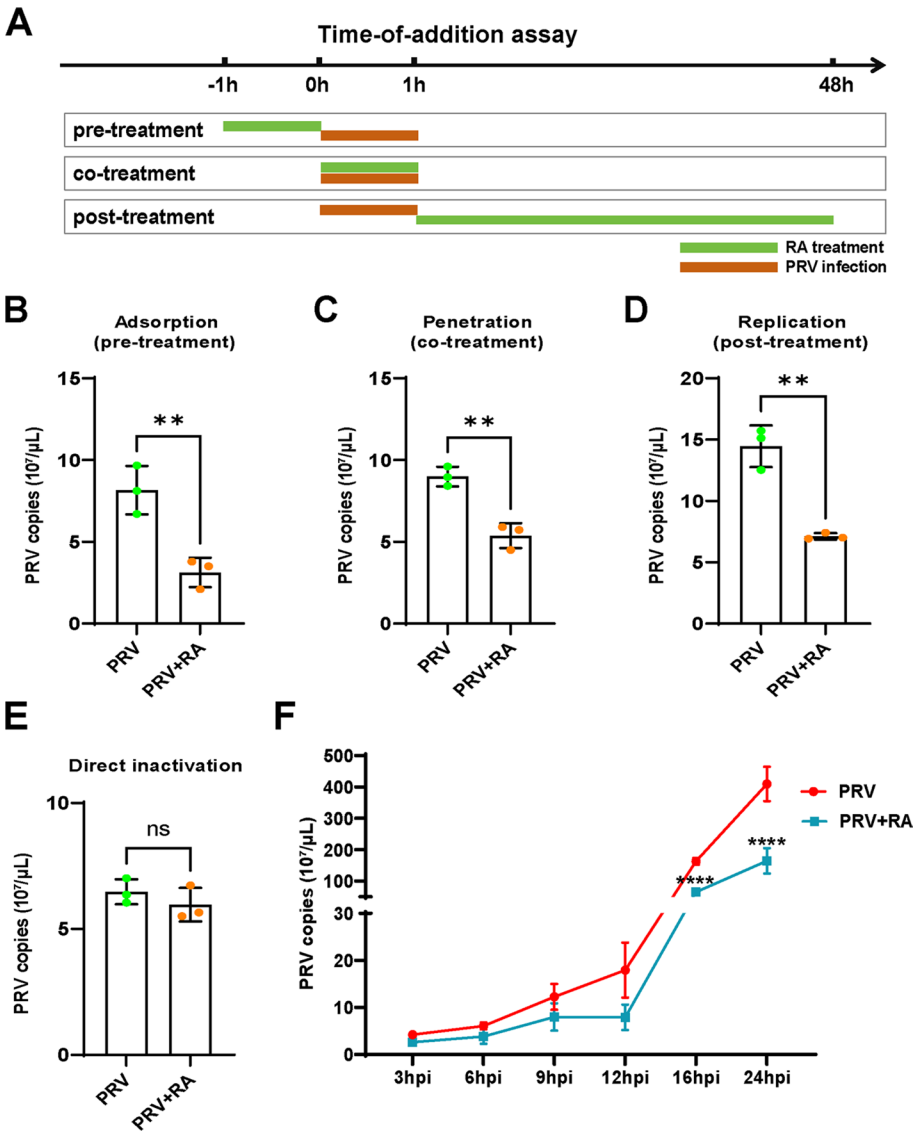

Fig. 2 Effects of RA on the PRV infection cycle and growth curve. **A** A time-of-addition assay was performed, where PK-15 cells were infected with PRV (100 $TCID_{50}$) for 1 h (0–1 h) and treated with RA (6 μg/mL) at different stages of infection, (**B**) adsorption (pre-treatment), (**C**) penetration (co-treatment), or (**D**) replication (post-treatment). Effect of RA on PRV direct inactivation (**E**) and viral growth curve (**F**). Statistical analyses for panels B–E were performed using unpaired t-tests, while panel F was analyzed using two-way ANOVA followed by Šidák's post-hoc test. *p*-values less than 0.05 were considered statistically significant (*$p < 0.05$, **$p < 0.01$, ***$p < 0.001$ and ****$p < 0.0001$ compared with the PRV group)

This indicates that RA may activate cGAS, thereby triggering the innate immune cGAS-STING signaling pathway, enhancing IFN-β expression, and exerting anti-PRV activity.

RA suppresses mRNA expression of inflammation and apoptosis-related genes induced by PRV

PRV infection triggers systemic inflammatory responses and apoptosis, leading to tissue damage in animals [45, 46]. The gene-expression levels of inflammation and apoptosis in PRV-infected PK-15 cells were determined via qRT-PCR. RA therapy significantly decreased the mRNA levels of inflammatory cytokines TNF-α, IL-1β, and IL-6 (Fig. 5A) compared with the PRV group. Furthermore, RA significantly reduced the mRNA expression of the pro-apoptotic factors Caspase-3 and Bax (Fig. 5B), while increasing the anti-apoptotic factor Bcl-2 (Fig. 5C).

RA improves survival rates and inhibits PRV replication in mice

This study assesses the therapeutic effects of RA in a PRV-infected mouse model (Fig. 6A). The LD_{50} calculated

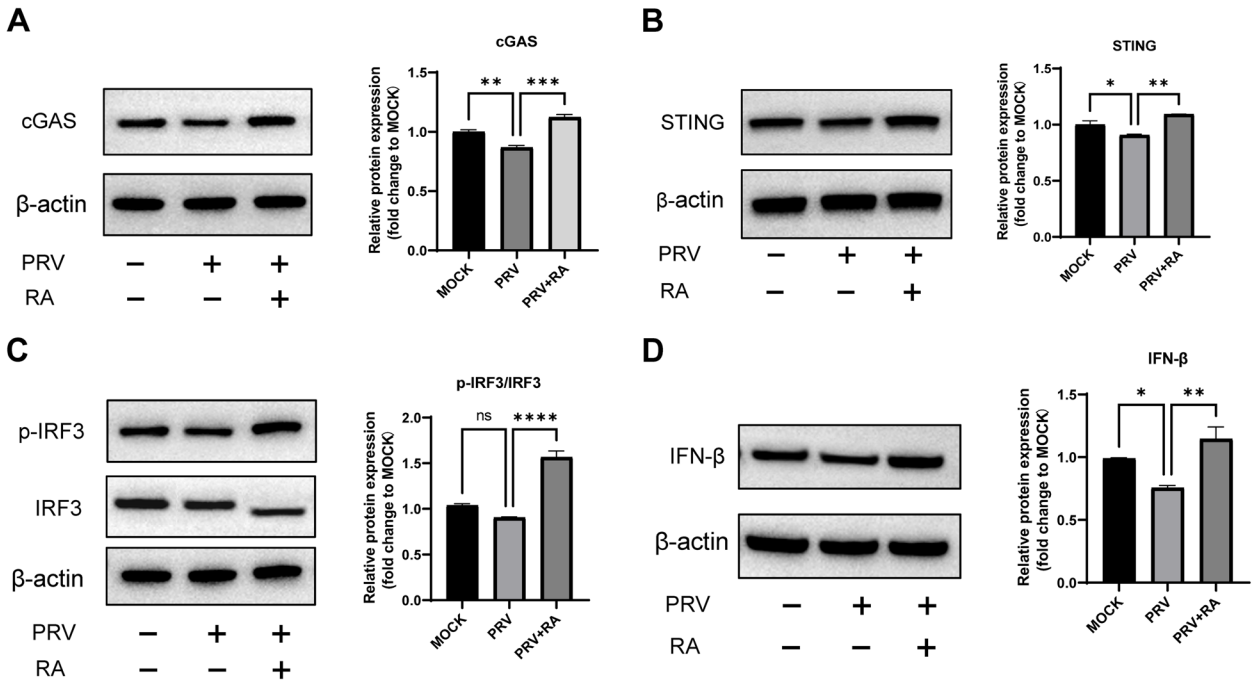

Fig. 3 Effect of RA on the expression of proteins related to the cGAS-STING signaling pathway and antiviral effector IFN-β in PK-15 cells post-PRV infection. Levels of cGAS (**A**), STING (**B**), p-IRF3 and IRF3 (**C**), and IFN-β (**D**) were analyzed by Western blotting. Relative protein expression (fold change compared to MOCK) was quantified using Image J software. Statistical analyses were performed using one-way ANOVA, followed by Dunnett's post-hoc test. *p*-values less than 0.05 were considered statistically significant (*$p < 0.05$, **$p < 0.01$, ***$p < 0.001$ and ****$p < 0.0001$ compared with the PRV group)

by the Reed-Muench formula was $10^{-4.2}$/100 μL, and mice were infected at this concentration to establish the infection model. After the third day post-infection, the PRV group displayed notable clinical symptoms, including frequent scratching, moist mouth corners, purulent eye discharge, severe lethargy, and ruffled fur. Mortality started on the fourth day. In the RA-L and RA-M groups, some mice displayed purulent eye discharge by the fourth day, whereas this symptom was not observed in the RA-H group. On the fifth day, mortality rates were 0, 60, 30, 10, and 0% in groups of MOCK, PRV, RA-L, RA-M, and RA-H, respectively (Fig. 6B).

Measurement of viral genome copies in mouse organs indicated that PRV replicates in multiple tissues, including the liver (Fig. 6C), kidneys (Fig. 6D), spleen (Fig. 6E), brain (Fig. 6F), lungs (Fig. 6G), and intestines (Fig. 6H), consistent with previous reports [47]. RA treatment significantly reduced viral copy numbers in a dose-dependent manner, particularly at medium and high doses, suggesting that RA effectively suppresses PRV replication.

RA effectively suppresses inflammation and apoptosis induced by PRV

PRV infection triggers an inflammatory response and apoptosis in animals, leading to tissue damage, including interstitial pneumonia [45]. The expression levels of inflammatory and apoptotic factors in mouse lung tissues were quantified using qRT-PCR. In PRV-infected mice, the mRNA expression levels of inflammatory factors TNF-α (Fig. 7A), IL-1β (Fig. 7B), and IL-6 (Fig. 7C), as well as apoptotic factors Caspase-3 (Fig. 7D) and Bax (Fig. 7E), were significantly elevated, whereas Bcl-2 (Fig. 7F) mRNA levels were notably reduced. RA treatment partially reversed these alterations, consistent with cellular-level results. The ELISA results further

(See figure on next page.)

Fig. 4 Molecular Docking and Dynamics Simulation of RA with cGAS and STING Proteins. Docking models of RA with cGAS (PDB: 4JLZ) (**A**) and STING (K7GKX5) (**B**) are depicted, with proteins in cartoon form, amino acid residues as blue sticks, RA in yellow, hydrogen bonds as blue lines, *π-π* stacking interactions as green dashed lines, salt bridges as yellow dashed lines, and hydrophobic interactions as gray dashed lines. The RMSD of the cGAS_RA (**C**) and STING_RA (**D**) complexes. The RMSF of the cGAS_RA (**E**) and STING_RA (**F**) complexes. **G** MM-GBSA binding free energy and energy decomposition analysis of RA with cGAS and STING, separately

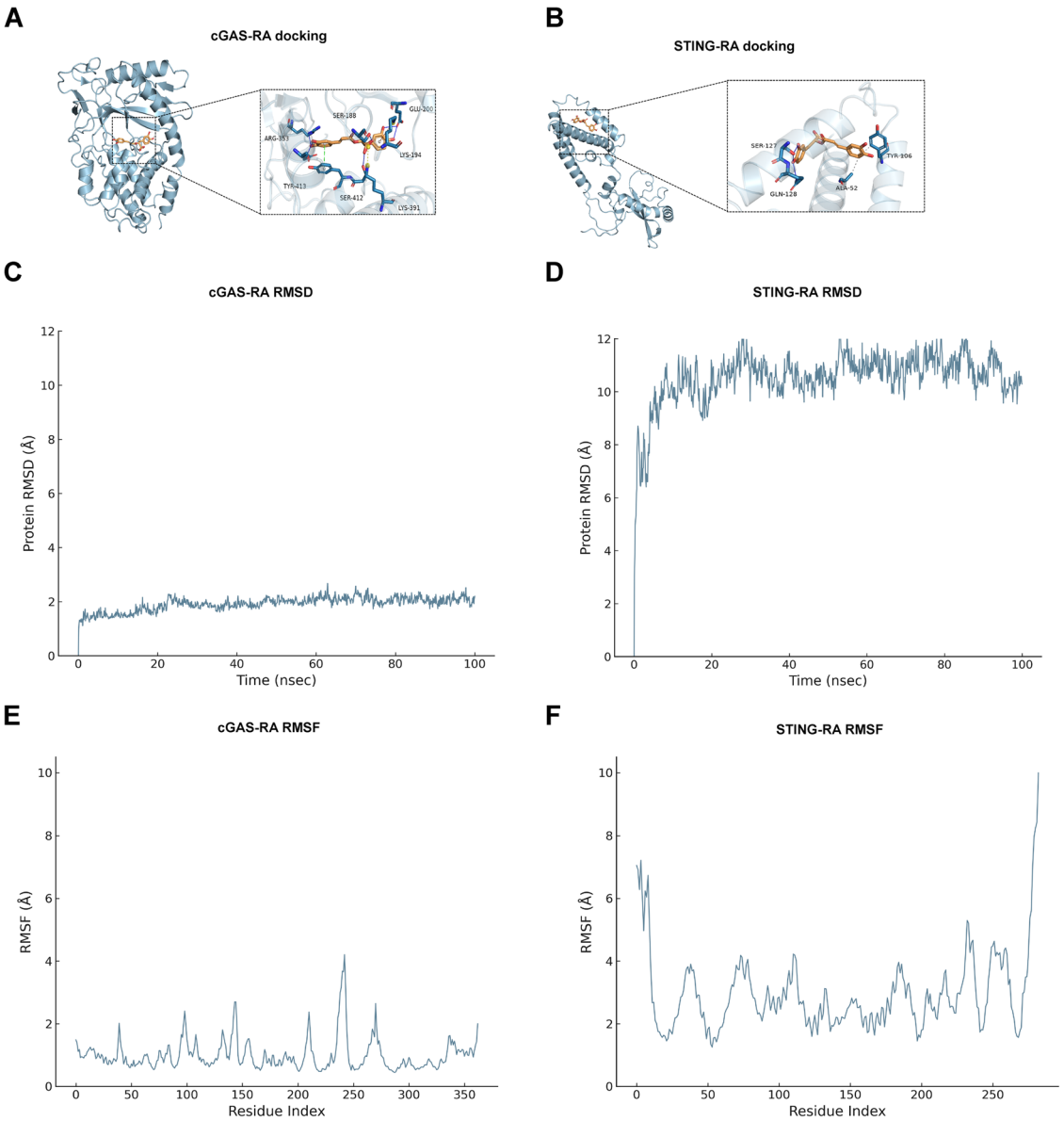

G

MM-GBSA parameters for the cGAS_ RA and STING_ RA complexes

Unit（kcal/mol）	cGAS_ RA	STING_ RA
Binding Free Energy (dG)	-51.4596	-64.7713
Coulombic Interaction Energy	-86.2365	-67.4368
Covalent Binding Free Energy	3.964615	1.485559
Hydrogen Bond Binding Energy	-2.30315	-1.76574
Lipophilic Stabilization Energy	-18.4559	-23.7031
Packing Interaction Energy	-2.32579	-2.15311
Electrostatic Solvation Energy (GB Model)	98.1078	73.61637
Lennard-Jones Potential Energy (vdW)	-44.2107	-44.8144

Fig. 4 (See legend on previous page.)

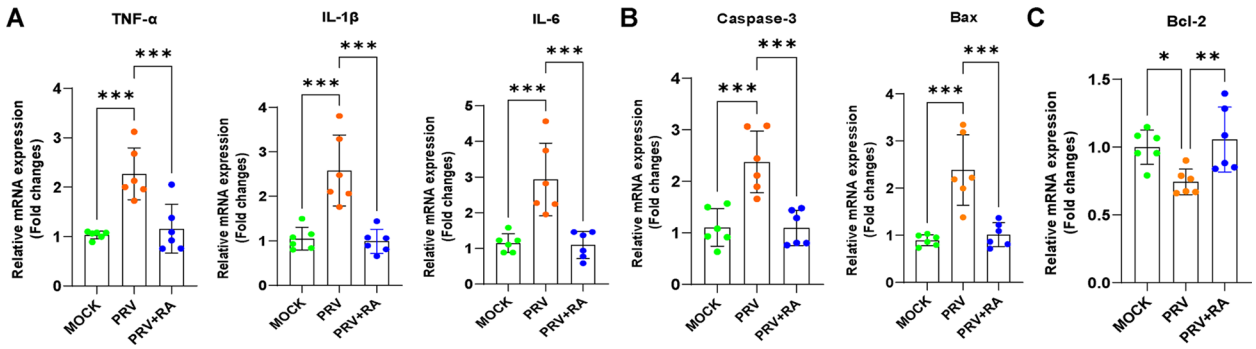

Fig. 5 Effect of RA (6 μg/mL) on inflammation and apoptosis related gene expression in PK-15 cells post-PRV infection. **A** mRNA levels of inflammatory cytokines TNF-α, IL-1β, and IL-6 analyzed by qRT-PCR. **B** mRNA levels of pro-apoptotic factors Caspase-3 and Bax analyzed by qRT-PCR. **C** mRNA levels of the anti-apoptotic factor Bcl-2 analyzed by qRT-PCR. Statistical analyses were performed using one-way ANOVA, followed by Dunnett's post-hoc test. *p*-values less than 0.05 were considered statistically significant (*$p < 0.05$, **$p < 0.01$, ***$p < 0.001$ and ****$p < 0.0001$ compared with the PRV group)

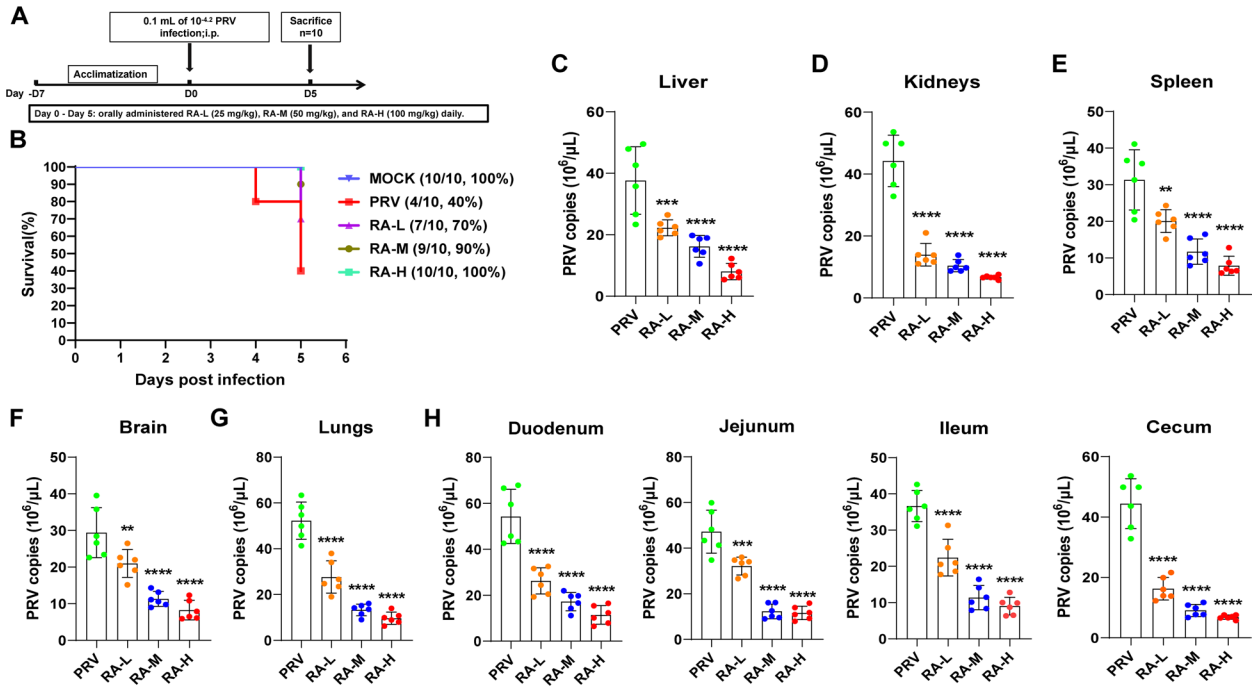

Fig. 6 Effect of RA on survival curves and tissue viral genome copies in PRV-infected mice. **A** Experimental design in mice. **B** The survival rates of mice treated with RA. Viral genome copies of the liver (**C**), kidneys (**D**), spleen (**E**), brain (**F**), lungs (**G**), and intestines (duodenum/jejunum/ileum/cecum) (**H**). Statistical analyses were performed using one-way ANOVA, followed by Dunnett's post-hoc test. *p*-values less than 0.05 were considered statistically significant (*$p < 0.05$, **$p < 0.01$, ***$p < 0.001$ and ****$p < 0.0001$ compared with the PRV group)

confirmed that RA effectively regulated inflammation and apoptosis in infected mice (Fig. 7G).

RA activates the cGAS-STING signaling pathway

Studies have demonstrated that viruses can impede the activation of the cGAS-STING pathway through mechanisms such as disrupting signaling, evading DNA recognition, and impairing immune cell function, thereby evading immune surveillance and enhancing their infectivity [18]. In this study, qRT-PCR was employed to assess the expression levels of the cGAS, STING, IRF3, and IFN-β genes in the lung tissues of infected mice. The findings reveal that RA effectively counteracts the suppression of the cGAS-STING pathway induced by PRV infection. RA significantly activates the cGAS-STING signaling pathway, markedly increasing the mRNA expression of cGAS (Fig. 8A), STING (Fig. 8B), and IRF3 (Fig. 8C). This

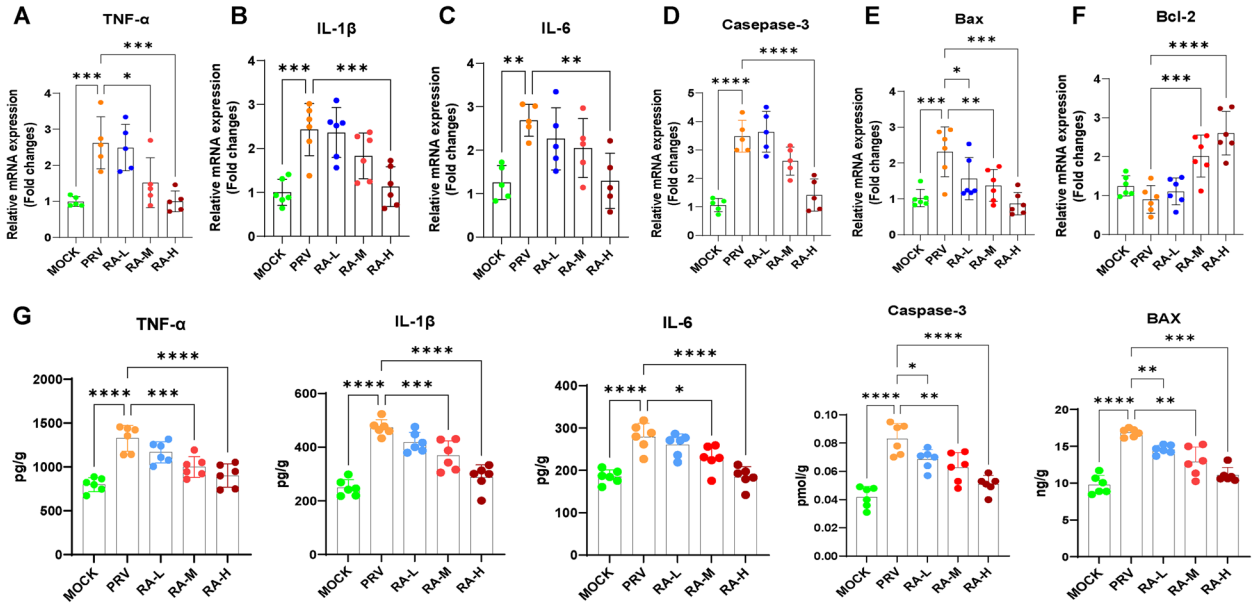

Fig. 7 Effect of RA on inflammation and apoptosis in mice. The mRNA expression levels of inflammatory cytokines TNF-α (**A**), IL-1β (**B**), and IL-6 (**C**), pro-apoptotic factors Caspase-3 (**D**) and Bax (**E**), and the anti-apoptotic factor Bcl-2 (**F**) were quantified using qRT-PCR, while protein expression was evaluated by ELISA (**G**). Statistical analyses were performed using one-way ANOVA, followed by Dunnett's post-hoc test. *p*-values less than 0.05 were considered statistically significant (*$p < 0.05$, **$p < 0.01$, ***$p < 0.001$ and ****$p < 0.0001$ compared with the PRV group)

activation subsequently enhances the expression of the antiviral effector IFN-β (Fig. 8D), thereby promoting an effective antiviral immune response.

Discussion

Natural small molecules, due to their extensive availability and low toxicity, have become a key focus in antiviral drug research [48]. RA is a natural polyphenol with diverse biological activities, including antioxidant, anti-inflammatory, antibacterial, antiviral, immunomodulatory, antitumor, and neuroprotective effects [49–53]. This study demonstrates that RA is a highly effective, low-toxicity small molecule (SI = 31.22), as evidenced by its cytotoxicity assay and antiviral activity against PRV in PK-15 cells.

TEM is the only imaging technique that directly visualizes viruses due to its nanometer-scale resolution, playing a crucial role in virus detection [54]. The antiviral activity of RA was further validated by TEM, which revealed ultrastructural damage in PRV-infected cells, including membrane rupture, irregular nuclear shape,

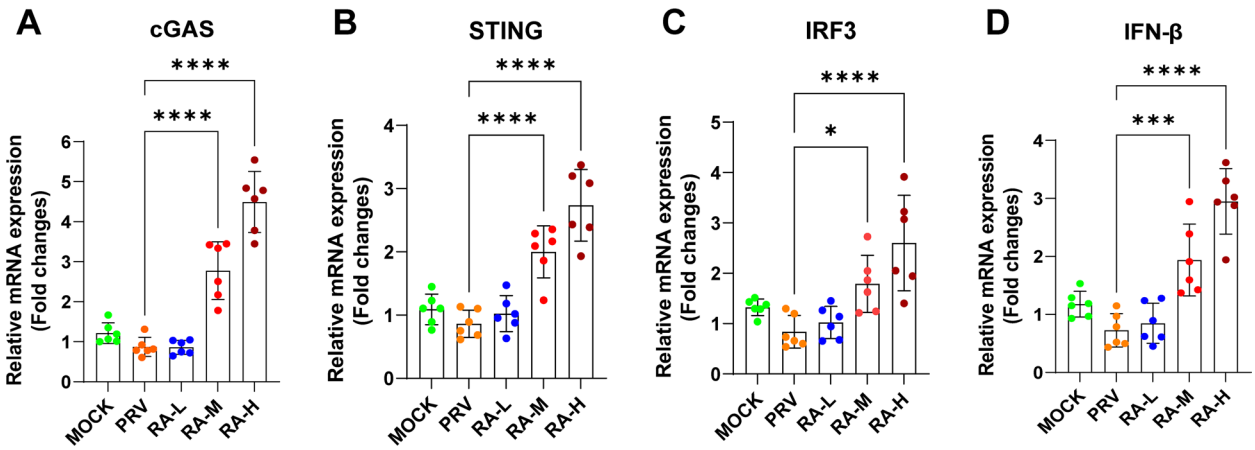

Fig. 8 The effect of RA on the expression of the cGAS-STING signaling pathway and the antiviral effector IFN-β in mice post-PRV infection. The mRNA levels of cGAS (**A**), STING (**B**), IRF3 (**C**), and IFN-β (**D**) were quantified by qRT-PCR. Statistical analyses were performed using one-way ANOVA, followed by Dunnett's post-hoc test. *p*-values less than 0.05 were considered statistically significant (*$p < 0.05$, **$p < 0.01$, ***$p < 0.001$ and ****$p < 0.0001$ compared with the PRV group)

mild chromatin loss, and viral particle aggregation within the nucleus. Mitochondrial swelling, matrix dissolution, vacuolation, reduced and sparse cristae, autolysosomes in the cytoplasm, and a large number of vesicles slightly dilated Golgi apparatus were also observed. However, cells treated with RA showed only mild mitochondrial swelling, suggesting that RA reduces viral genome copies and ultrastructural damage in infected cells.

The viral life cycle can be divided into stages such as adsorption, penetration, replication, and gene expression, each involving interactions with the host cell [55]. The time-of-addition assay is a crucial method in antiviral drug research, designed to identify the stage of the viral infection cycle at which a drug exerts its effect. By analyzing the inhibitory effects at different stages, the potential targets of the drug can be inferred [56]. The findings reveal that, although RA did not demonstrate significant direct virucidal activity against PRV, it markedly inhibited viral adsorption, penetration, and replication within PK-15 cells. This suggests that RA may not function as a direct antiviral agent but rather interferes with virus-host cell interactions.

The cGAS-STING signaling pathway plays a crucial role in the immune response against DNA viruses [57], but PRV has evolved several mechanisms to evade host cGAS-STING-mediated antiviral recognition. For instance, PRV tegument protein UL13 inhibits this pathway by promoting the ubiquitin-mediated degradation of STING [25]. Additionally, PRV glycoprotein E (gE) disrupts the assembly of the IRF3-CBP enhancer complex by degrading CBP, thereby suppressing cGAS-STING-mediated IFN-β production [29]. To determine whether RA exerts its antiviral effects through the cGAS-STING signaling pathway, Western blot analysis was conducted to assess the expression levels of pathway proteins in PRV-infected PK-15 cells. The results showed that PRV infection inhibited the cGAS-STING pathway. However, treatment with RA reversed this inhibition, significantly activating the cGAS-STING pathway and elevating the expression of IFN-β.

To verify the binding of RA to cGAS and STING proteins, we employed molecular docking and molecular dynamics simulation methods. Molecular docking provides rapid insights into binding modes and affinity estimates, while molecular dynamics simulation reveals the behavior and stability of the molecular complex during dynamic processes, offering validation for molecular mechanism studies and drug design [58, 59]. Molecular docking results revealed that the binding scores for the cGAS_RA and STING_RA complexes were both below −5, indicating strong interactions between RA and the cGAS and STING proteins. Subsequent molecular dynamics simulations confirmed higher binding stability of RA with cGAS compared to STING, suggesting RA potential as a cGAS activator.

PRV has a broad host range, capable of infecting almost all mammals, which has enabled researchers to develop various animal models of infection. Mice and rabbits are often chosen as ideal experimental animals due to their physiological properties and ease of care. Infection methods can be selected based on the experimental objectives, including intranasal, intraperitoneal, intramuscular, footpad, and subcutaneous injections [60]. In this study, an intraperitoneal injection of PRV successfully established a PRV-infected mouse model. Analysis of survival rates and clinical symptoms revealed that RA significantly alleviated viral infection symptoms and reduced mortality, with no deaths observed in the high-dose group, further demonstrating RA effectiveness in treating PRV infection. The tissue distribution of PRV in mouse models is a critical parameter. In this study, PRV was found to replicate in the liver, kidneys, spleen, brain, lungs, and intestines, consistent with prior reports [47]. The increased viral genome copies of PRV in the brain can be attributed to its neurotropism. After RA treatment, a significant reduction in viral genome copies was observed, indicating that RA inhibits PRV replication in vivo in a dose-dependent manner. To further validate RA potential as a cGAS activator, qRT-PCR was used to assess the expression of cGAS-STING pathway genes and IFN-β in lung tissues, showing a significant dose-dependent upregulation of cGAS, STING, IRF3, and IFN-β, consistent with in vitro findings.

PRV infection induces inflammatory responses and apoptosis [46]. Specifically, the PRV UL4 protein manipulates host cells inflammatory signaling and apoptosis to enhance pathogenicity [61]. In PK-15 cells, PRV infection triggers oxidative stress signaling, leading to apoptosis [62]. In this study, PRV infection resulted in significant inflammatory responses and apoptosis both in vitro and in vivo. Subsequent to RA treatment, the inflammation and apoptosis induced by PRV were effectively reduced. Literature indicates that RA can block caspase-1 activity, inhibiting the expression of apoptotic and anti-apoptotic factors, as well as NF-κB activation, thereby exerting anti-inflammatory and anti-apoptotic effects [63]. Furthermore, RA suppresses the activation of the NLRP3 inflammasome signaling pathway [40]. These findings provide a theoretical basis for the ability of RA to suppress PRV-induced inflammation and apoptosis. However, the precise molecular mechanisms involved remain unclear and warrant further investigation.

Although the mouse infection model provided valuable insights into the basic biological mechanisms of RA against PRV, it has limitations. Mice are not the natural

host of PRV, and the infection patterns and clinical features may differ from those in natural hosts. These interspecies differences could affect the comprehensive evaluation of RA antiviral efficacy. Furthermore, PRV can establish latent infections, allowing it to persist within the host, where stressful stimuli may induce viral reactivation [2]. This phenomenon could impact the therapeutic efficacy of RA. Therefore, it is crucial to investigate the interactions between RA and key proteins involved in PRV latency and reactivation in vitro [64], as well as to conduct efficacy evaluations in vivo [65]. Overall, further validation of the antiviral potential and mechanisms of RA is essential to strengthen the theoretical foundation for its development as an antiviral drug. Additionally, the ability of RA to activate the cGAS-STING pathway suggests its potential as a broad-spectrum antiviral agent against other DNA viruses.

Supplementary Information

The online version contains supplementary material available at https://doi.org/10.1186/s12866-024-03732-4.

Supplementary Material 1.

Supplementary Material 2.

Acknowledgements
The authors would like to thank the personnel of these teams for their kind assistance.

Clinical trial number
Not applicable.

Authors' contributions
CRediT authorship contribution statement: Tingting Hu and Sihui Gao: Conceptualization, Data curation, Formal analysis, Methodology, Validation, Visualization, Writing - original draft. Zhijie Yu and Yunhao Liu: Formal analysis, Investigation. Huaqiao Tang, Zhiwen Xu, Ling Zhu, Ling Zhao and Gang Ye: Investigation, Methodology, Resources. Fei Shi: Supervision, Project administration, Methodology, Validation, Visualization, Writing - editing.

Funding
The study was funded by the Key Open Laboratory of the National People's Committee (Grant No. [2022]08).

Data availability
All data generated or analysed during this study are included in this published article.

Declarations

Ethics approval and consent to participate
This study was approved by the Animal Protection and Experimental Ethics Committee of Sichuan Agricultural University (Sichuan, China, approval No.20230045).

Consent for publication
Not applicable.

Competing interests
The authors declare no competing interests.

Author details
[1]College of Veterinary Medicine, Sichuan Agricultural University, Chengdu 611130, China.

Received: 3 September 2024 Accepted: 23 December 2024
Published online: 17 March 2025

References

1. Mettenleiter TC. Aujeszky's disease (pseudorabies) virus: the virus and molecular pathogenesis–state of the art, June 1999. Vet Res. 2000;31(1):99–115.
2. Pomeranz LE, Reynolds AE, Hengartner CJ. Molecular biology of pseudorabies virus: impact on neurovirology and veterinary medicine. Microbiol Mol Biology Reviews: MMBR. 2005;69(3):462–500.
3. Pedersen K, Turnage CT, Gaston WD, Arruda P, Alls SA, Gidlewski T. Pseudorabies detected in hunting dogs in Alabama and Arkansas after close contact with feral swine (Sus scrofa). BMC Vet Res. 2018;14(1):388.
4. Bo Z, Li X. A review of Pseudorabies Virus variants: Genomics, Vaccination, Transmission, and zoonotic potential. Viruses. 2022;14(5):1003.
5. Hitl M, Kladar N, Gavarić N, Božin B. Rosmarinic Acid-Human pharmacokinetics and Health benefits. Planta Med. 2021;87(4):273–82.
6. Colica C, Di Renzo L, Aiello V, De Lorenzo A, Abenavoli L. Rosmarinic acid as potential anti-inflammatory Agent. Rev Recen Clin Trial. 2018;13(4):240–2.
7. Kernou ON, Azzouz Z, Madani K, Rijo P. Application of Rosmarinic Acid with its derivatives in the treatment of Microbial pathogens. Molecules. 2023;28(10):4243.
8. Zhao J, Xu L, Jin D, Xin Y, Tian L, Wang T, Zhao D, Wang Z, Wang J. Rosmarinic acid and related dietary supplements: potential applications in the Prevention and Treatment of Cancer. Biomolecules. 2022;12(10):1410.
9. Tsukamoto Y, Ikeda S, Uwai K, Taguchi R, Chayama K, Sakaguchi T, Narita R, Yao WL, Takeuchi F, Otakaki Y, et al. Rosmarinic acid is a novel inhibitor for Hepatitis B virus replication targeting viral epsilon RNA-polymerase interaction. PLoS ONE. 2018;13(5):e0197664.
10. Jheng JR, Hsieh CF, Chang YH, Ho JY, Tang WF, Chen ZY, Liu CJ, Lin TJ, Huang LY, Chern JH, et al. Rosmarinic acid interferes with influenza virus a entry and replication by decreasing GSK3β and phosphorylated AKT expression levels. J Microbiol Immunol Infect. 2022;55(4):598–610.
11. Zhou B, Wang L, Yang S, Liang Y, Zhang Y, Pan X, Li J. Rosmarinic acid treatment protects against lethal H1N1 virus-mediated inflammation and lung injury by promoting activation of the h-PGDS-PGD(2)-HO-1 signal axis. Chin Med. 2023;18(1):139.
12. Swarup V, Ghosh J, Ghosh S, Saxena A, Basu A. Antiviral and anti-inflammatory effects of rosmarinic acid in an experimental murine model of Japanese encephalitis. Antimicrob Agents Chemother. 2007;51(9):3367–70.
13. Weng JY, Chen XX, Wang XH, Ye HE, Wu YP, Sun WY, Liang L, Duan WJ, Kurihara H, Huang F, et al. Reducing lipid peroxidation attenuates stress-induced susceptibility to herpes simplex virus type 1. Acta Pharmacol Sin. 2023;44(9):1856–66.
14. Sun L, Wu J, Du F, Chen X, Chen ZJ. Cyclic GMP-AMP synthase is a cytosolic DNA sensor that activates the type I interferon pathway. Sci (New York NY). 2013;339(6121):786–91.
15. Ishikawa H, Ma Z, Barber GN. STING regulates intracellular DNA-mediated, type I interferon-dependent innate immunity. Nature. 2009;461(7265):788–92.
16. Zhao C, Zhao W. TANK-binding kinase 1 as a novel therapeutic target for viral diseases. Expert Opin Ther Targets. 2019;23(5):437–46.
17. Sin WX, Li P, Yeong JP, Chin KC. Activation and regulation of interferon-β in immune responses. Immunol Res. 2012;53(1–3):25–40.
18. Ge Z, Ding S. Regulation of cGAS/STING signaling and corresponding immune escape strategies of viruses. Front Cell Infect Microbiol. 2022;12:954581.
19. Ding C, Song Z, Shen A, Chen T, Zhang A. Small molecules targeting the innate immune cGAS–STING–TBK1 signaling pathway. Acta Pharm Sinica B. 2020;10(12):2272–98.
20. Zhang J, Zhao J, Xu S, Li J, He S, Zeng Y, Xie L, Xie N, Liu T, Lee K, et al. Species-specific deamidation of cGAS by herpes Simplex Virus UL37 protein facilitates viral replication. Cell Host Microbe. 2018;24(2):234–e248235.

21. Su C, Zheng C. Herpes Simplex Virus 1 abrogates the cGAS/STING-Mediated cytosolic DNA-Sensing pathway via its virion host shutoff protein, UL41. J Virol. 2017;91(6):e02414-16.
22. Zhang Y, Li M, Li L, Qian G, Wang Y, Chen Z, Liu J, Fang C, Huang F, Guo D, et al. β-arrestin 2 as an activator of cGAS-STING signaling and target of viral immune evasion. Nat Commun. 2020;11(1):6000.
23. Bodda C, Reinert LS, Fruhwürth S, Richardo T, Sun C, Zhang BC, Kalamvoki M, Pohlmann A, Mogensen TH, Bergström P et al. HSV1 VP1-2 deubiquitinates STING to block type I interferon expression and promote brain infection. J Exp Med/ 2020;217(7):20191422.
24. Zhang D, Su C, Zheng C. Herpes Simplex Virus 1 serine protease VP24 blocks the DNA-Sensing Signal Pathway by Abrogating Activation of Interferon Regulatory Factor 3. J Virol. 2016;90(12):5824–9.
25. Kong Z, Yin H, Wang F, Liu Z, Luan X, Sun L, Liu W, Shang Y. Pseudorabies virus tegument protein UL13 recruits RNF5 to inhibit STING-mediated antiviral immunity. PLoS Pathog. 2022;18(5):e1010544.
26. Bo Z, Miao Y, Xi R, Zhong Q, Bao C, Chen H, Sun L, Qian Y, Jung YS, Dai J. PRV UL13 inhibits cGAS-STING-mediated IFN-β production by phosphorylating IRF3. Vet Res. 2020;51(1):118.
27. Yan Z, Xie J, Hou Z, Zhang Y, Yue J, Zhang X, Chen L, Yang Y, Li X, Li H, et al. Pseudorabies virus UL38 attenuates the cGAS-STING signaling pathway by recruiting Tollip to promote STING for autophagy degradation. Virol J. 2024;21(1):107.
28. Kong Z, Chen X, Gong L, Wang L, Zhang Y, Guan K, Yao W, Kang Y, Lu X, Zhang Y, et al. Pseudorabies virus tegument protein US2 antagonizes antiviral innate immunity by targeting cGAS-STING signaling pathway. Front Immunol. 2024;15:1403070.
29. Lu M, Qiu S, Zhang L, Sun Y, Bao E, Lv Y. Pseudorabies virus glycoprotein gE suppresses interferon-β production via CREB-binding protein degradation. Virus Res. 2021;291:198220.
30. Lei C, Yang J, Hu J, Sun X. On the calculation of TCID(50) for quantitation of Virus Infectivity. Virol Sin. 2021;36(1):141–4.
31. Pirzada RH, Haseeb M, Batool M, Kim M, Choi S. Remdesivir and Ledipasvir among the FDA-Approved antiviral drugs have potential to inhibit SARS-CoV-2 replication. Cells. 2021;10(5):1052.
32. Ramesh AK, Parreño V, Schmidt PJ, Lei S, Zhong W, Jiang X, Emelko MB, Yuan L. Evaluation of the 50% infectious dose of human norovirus Cin-2 in Gnotobiotic pigs: a comparison of classical and contemporary methods for Endpoint Estimation. Viruses. 2020;12(9):E955.
33. Liu X, Song Z, Bai J, Nauwynck H, Zhao Y, Jiang P. Xanthohumol inhibits PRRSV proliferation and alleviates oxidative stress induced by PRRSV via the Nrf2-HMOX1 axis. Vet Res. 2019;50(1):61.
34. Li Z, He Y, Ge L, Quan R, Chen J, Hu Y, Sa R, Liu J, Ran D, Fu Q, et al. Berbamine, a bioactive alkaloid, suppresses equine herpesvirus type 1 in vitro and in vivo. Front Veterinary Sci. 2023;10:1163780.
35. Bass JJ, Wilkinson DJ, Rankin D, Phillips BE, Szewczyk NJ, Smith K, Atherton PJ. An overview of technical considerations for Western blotting applications to physiological research. Scand J Med Sci Sports. 2017;27(1):4–25.
36. Gallo-Oller G, Ordoñez R, Dotor J. A new background subtraction method for Western blot densitometry band quantification through image analysis software. J Immunol Methods. 2018;457:1–5.
37. Pagadala NS, Syed K, Tuszynski J. Software for molecular docking: a review. Biophys Rev. 2017;9(2):91–102.
38. Kontoyianni M. Docking and virtual screening in Drug Discovery. Methods Mol Biology (Clifton NJ). 2017;1647:255–66.
39. Samy CRA, Karunanithi K, Sheshadhri J, Rengarajan M, Srinivasan P, Cherian P. (R)-(+)-Rosmarinic acid as an inhibitor of herpes and Dengue Virus Replication: an in Silico Assessment. Revista brasileira de farmacognosia: orgao oficial da Sociedade Brasileira de Farmacognosia. 2023;33(3):543–50.
40. Akhter J, Khan J, Baghel M, Beg MMA, Goswami P, Afjal MA, Ahmad S, Habib H, Najmi AK, Raisuddin S. NLRP3 inflammasome in rosmarinic acid-afforded attenuation of acute kidney injury in mice. Sci Rep. 2022;12(1):1313.
41. Song K, Yu JY, Li J, Li M, Peng LY, Yi PF. Astragaloside IV regulates cGAS-STING signaling pathway to alleviate Immunosuppression caused by PRRSV infection. Viruses. 2023;15(7):1586.
42. Chen Z, Wang W, Zeng K, Zhu J, Wang X, Huang W. Potential antiviral activity of rhamnocitrin against influenza virus H3N2 by inhibiting cGAS/STING pathway in vitro. Sci Rep. 2024;14(1):28287.
43. Qi H, Ma QH, Feng W, Chen SM, Wu CS, Wang Y, Wang TX, Hou YL, Jia ZH. Glycyrrhetinic acid blocks SARS-CoV-2 infection by activating the cGAS-STING signalling pathway. Br J Pharmacol. 2024;181(20):3976–92.
44. Tuccinardi T. What is the current value of MM/PBSA and MM/GBSA methods in drug discovery? Expert Opin Drug Discov. 2021;16(11):1233–7.
45. Sehl J, Teifke JP. Comparative Pathology of pseudorabies in different naturally and experimentally infected Species-A Review. Pathogens (Basel Switzerland). 2020;9(8):E633.
46. Sun M, Hou L, Song H, Lyu C, Tang YD, Qin L, Liu Y, Wang S, Meng F, Cai X. The relationship between autophagy and apoptosis during pseudorabies virus infection. Front Veterinary Sci. 2022;9:1064433.
47. Ren CZ, Hu WY, Zhang JW, Wei YY, Yu ML, Hu TJ. Establishment of inflammatory model induced by Pseudorabies virus infection in mice. J Vet Sci. 2021;22(2):e20.
48. Li W, Wang XH, Luo Z, Liu LF, Yan C, Yan CY, Chen GD, Gao H, Duan WJ, Kurihara H et al. Traditional Chinese medicine as a potential source for HSV-1 therapy by acting on Virus or the susceptibility of host. Int J Mol Sci. 2018;19(10):3266.
49. Alagawany M, Abd El-Hack ME, Farag MR, Gopi M, Karthik K, Malik YS, Dhama K. Rosmarinic acid: modes of action, medicinal values and health benefits. Anim Health Res Rev. 2017;18(2):167–76.
50. Ghasemzadeh Rahbardar M, Hosseinzadeh H. Effects of rosmarinic acid on nervous system disorders: an updated review. Naunyn Schmiedebergs Arch Pharmacol. 2020;393(10):1779–95.
51. Yesilbag D, Eren M, Agel H, Kovanlikaya A, Balci F. Effects of dietary rosemary, rosemary volatile oil and vitamin E on broiler performance, meat quality and serum SOD activity. Br Poult Sci. 2011;52(4):472–82.
52. Nascimento RF do, Oliveira Formiga R de, Machado FDF, Sales IRP de, Lima GM de, Alves Júnior EB, Vieira GC, Pereira RF, Araújo AA de. Araújo Junior RF de. Rosmarinic acid prevents gastric ulcers via sulfhydryl groups reinforcement, antioxidant and immunomodulatory effects. Naunyn Schmiedebergs Arch Pharmacol. 2020;393(12):2265–2278.
53. Alkam T, Nitta A, Mizoguchi H, Itoh A, Nabeshima T. A natural scavenger of peroxynitrites, rosmarinic acid, protects against impairment of memory induced by Abeta(25–35). Behav Brain Res. 2007;180(2):139–45.
54. Roingeard P, Raynal PI, Eymieux S, Blanchard E. Virus detection by transmission electron microscopy: still useful for diagnosis and a plus for biosafety. Rev Med Virol. 2019;29(1):e2019.
55. Xia X, Cheng A, Wang M, Ou X, Sun D, Mao S, Huang J, Yang Q, Wu Y, Chen S, et al. Functions of viroporins in the viral life cycle and their regulation of host cell responses. Front Immunol. 2022;13:890549.
56. Šudomová M, Hassan STS. Flavonoids with anti-herpes Simplex Virus properties: deciphering their mechanisms in disrupting the viral life cycle. Viruses. 2023;15(12):2340.
57. Wang C, Guan Y, Lv M, Zhang R, Guo Z, Wei X, Du X, Yang J, Li T, Wan Y, et al. Manganese increases the sensitivity of the cGAS-STING pathway for double-stranded DNA and is required for the Host Defense against DNA viruses. Immunity. 2018;48(4):675–e687677.
58. Zhang J, Li F, Shen S, Yang Z, Ji X, Wang X, Liao X, Zhang Y. More simple, efficient and accurate food research promoted by intermolecular interaction approaches: a review. Food Chem. 2023;416:135726.
59. Fatriansyah JF, Rizqillah RK, Yandi MY, Fadilah, Sahlan M. Molecular docking and dynamics studies on propolis sulabiroin-A as a potential inhibitor of SARS-CoV-2. J King Saud Univ Sci. 2022;34(1):101707.
60. Hong W, Xiao S, Zhou R, Fang L, He Q, Wu B, Zhou F, Chen H. Protection induced by intramuscular immunization with DNA vaccines of pseudorabies in mice, rabbits and piglets. Vaccine. 2002;20(7–8):1205–14.
61. Zhang X, Chen G, Yin J, Nie L, Li L, Du Q, Tong D, Huang Y. Pseudorabies Virus UL4 protein promotes the ASC-dependent inflammasome activation and pyroptosis to exacerbate inflammation. PLoS Pathog. 2024;20(9):e1012546.
62. Lai IH, Chang CD, Shih WL. Apoptosis induction by Pseudorabies Virus via oxidative stress and subsequent DNA damage signaling. Intervirology. 2019;62(3–4):116–23.
63. Jeong HJ, Choi Y, Kim MH, Kang IC, Lee JH, Park C, Park R, Kim HM. Rosmarinic acid, active component of Dansam-Eum attenuates ototoxicity of cochlear hair cells through blockage of caspase-1 activity. PLoS ONE. 2011;6(4):e18815.

64. Pan L, Li M, Zhang X, Xia Y, Mian AM, Wu H, Sun Y, Qiu HJ. Establishment of an in vitro model of pseudorabies Virus latency and reactivation and identification of key viral latency-Associated genes. Viruses. 2023;15(3):808.
65. Li LT, Liu J, Luo M, Liu JS, Zhang MM, Zhang WJ, Chen HC, Liu ZF. Establishment of pseudorabies virus latency and reactivation model in mice dorsal root ganglia culture. J Gen Virol. 2023;104(11).

Publisher's Note

Springer Nature remains neutral with regard to jurisdictional claims in published maps and institutional affiliations.